

## Assessment of solid/liquid equilibria in the (U, Zr)O<sub>2+y</sub> system

Mastromarino, S.; Seibert, AF; Hashem, E.; Ciccioli, A.; Prieur, Damien; Scheinost, Andreas C.; Stohr, S.; Lajarge, P; Boshoven, JG; Robba, D.

**DOI**

[10.1016/j.jnucmat.2017.07.045](https://doi.org/10.1016/j.jnucmat.2017.07.045)

**Publication date**

2017

**Document Version**

Final published version

**Published in**

Journal of Nuclear Materials

**Citation (APA)**

Mastromarino, S., Seibert, AF., Hashem, E., Ciccioli, A., Prieur, D., Scheinost, A. C., Stohr, S., Lajarge, P., Boshoven, JG., Robba, D., Ernstberger, M., Bottomley, D., & Manara, D. (2017). Assessment of solid/liquid equilibria in the (U, Zr)O<sub>2+y</sub> system. *Journal of Nuclear Materials*, 494, 368-379.  
<https://doi.org/10.1016/j.jnucmat.2017.07.045>

**Important note**

To cite this publication, please use the final published version (if applicable).  
Please check the document version above.

**Copyright**

Other than for strictly personal use, it is not permitted to download, forward or distribute the text or part of it, without the consent of the author(s) and/or copyright holder(s), unless the work is under an open content license such as Creative Commons.

**Takedown policy**

Please contact us and provide details if you believe this document breaches copyrights.  
We will remove access to the work immediately and investigate your claim.



## Assessment of solid/liquid equilibria in the (U, Zr)O<sub>2+y</sub> system



S. Mastromarino<sup>a, b, c</sup>, A. Seibert<sup>a</sup>, E. Hashem<sup>a</sup>, A. Ciccioli<sup>b</sup>, D. Prieur<sup>a</sup>, A. Scheinost<sup>d</sup>,  
S. Stohr<sup>a</sup>, P. Lajarge<sup>a</sup>, J. Boshoven<sup>a</sup>, D. Robba<sup>a</sup>, M. Ernstberger<sup>a</sup>, D. Bottomley<sup>a</sup>,  
D. Manara<sup>a, \*</sup>

<sup>a</sup> European Commission, Joint Research Centre (JRC), Directorate of Nuclear Safety and Security, P.O. Box 2340, D-76125 Karlsruhe, Germany

<sup>b</sup> Università "La Sapienza", Department of Chemical Physics, Piazzale Aldo Moro 1, 00100 Rome, Italy

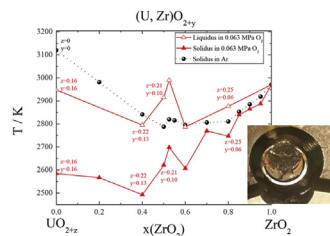
<sup>c</sup> Nuclear Energy and Radiation Applications (NERA), Radiation, Science & Technology Department, Faculty of Applied Sciences, Delft University of Technology, Mekelweg 15, 2629 JB Delft, The Netherlands

<sup>d</sup> Helmholtz Zentrum Dresden Rossendorf (HZDR), Institute of Resource Ecology, P.O. Box 10119, 01314 Dresden, Germany

### HIGHLIGHTS

- Solid/liquid equilibria in the whole UO<sub>2</sub>–ZrO<sub>2</sub> system are experimentally revisited for the first time since the 1950s.
- Air oxidation of mixed (U,Zr) dioxides has been studied by XANE spectroscopy for the first time.
- Solidus points have been obtained for hyperstoichiometric dioxide compositions of the type (U,Zr)O<sub>2+x</sub>.

### GRAPHICAL ABSTRACT



### ARTICLE INFO

#### Article history:

Received 7 April 2017

Received in revised form

23 May 2017

Accepted 24 July 2017

Available online 26 July 2017

#### Keywords:

Corium  
Core meltdown  
Laser heating  
Nuclear fuel  
Uranium dioxide  
Zirconium dioxide

### ABSTRACT

Solid/liquid equilibria in the system UO<sub>2</sub>–ZrO<sub>2</sub> are revisited in this work by laser heating coupled with fast optical thermometry. Phase transition points newly measured under inert gas are in fair agreement with the early measurements performed by Wisnyi et al., in 1957, the only study available in the literature on the whole pseudo-binary system. In addition, a minimum melting point is identified here for compositions near (U<sub>0.6</sub>Zr<sub>0.4</sub>)O<sub>2+y</sub>, around 2800 K. The solidus line is rather flat on a broad range of compositions around the minimum. It increases for compositions closer to the pure end members, up to the melting point of pure UO<sub>2</sub> (3130 K) on one side and pure ZrO<sub>2</sub> (2970 K) on the other. Solid state phase transitions (cubic-tetragonal-monoclinic) have also been observed in the ZrO<sub>2</sub>-rich compositions X-ray diffraction. Investigations under 0.3 MPa air (0.063 MPa O<sub>2</sub>) revealed a significant decrease in the melting points down to 2500 K–2600 K for increasing uranium content ( $x(\text{UO}_2) > 0.2$ ). This was found to be related to further oxidation of uranium dioxide, confirmed by X-ray absorption spectroscopy. For example, a typical oxidised corium composition U<sub>0.6</sub>Zr<sub>0.4</sub>O<sub>2.13</sub> was observed to solidify at a temperature as low as 2493 K.

The current results are important for assessing the thermal stability of the system fuel – cladding in an oxide based nuclear reactor, and for simulating the system behaviour during a hypothetical severe accident.

© 2017 The Authors. Published by Elsevier B.V. This is an open access article under the CC BY license (<http://creativecommons.org/licenses/by/4.0/>).

## 1. Introduction

In a nuclear reactor severe accident, particularly a loss-of-

\* Corresponding author.

E-mail address: [dario.manara@ec.europa.eu](mailto:dario.manara@ec.europa.eu) (D. Manara).

coolant accident (LOCA), the fuel is expected to be exposed to temperatures higher than 3000 K. At this temperature the fuel will therefore melt and react with the surrounding structural materials of the reactor such as the cladding, usually made of Zircaloy in water cooled thermal reactors, to form a reaction mixture commonly termed “corium” [1]. Corium is initially mostly composed of the highly refractory oxides  $\text{UO}_2$ , the molten fuel, and  $\text{ZrO}_2$  formed by the oxidation of the Zircaloy cladding with cooling water at high temperature. In further stages of a LOCA accident, more constituents would become part of the corium mass following its interaction with the structural materials of the reactor, mostly steel and concrete. Interaction between cladding material and fuel starts at approximately 1237 K [2]. In the same temperature range, fuel cladding and structural steels start to form eutectics [3] such as between Ni and Zr. The pure Zircaloy cladding melts at a higher temperature (~2123 K) and the  $\text{UO}_2$  fuel melts at much higher temperature to form a  $\text{U}_{1-x}\text{Zr}_x\text{O}_2$  liquid solution. Typical corium compositions have been observed to fall between  $\text{U}_{0.6}\text{Zr}_{0.4}\text{O}_{2+y}$  and  $\text{U}_{0.4}\text{Zr}_{0.6}\text{O}_{2+y}$ , so this range has been more broadly studied in this work as well as in previous literature. The melting-freezing behaviour on the entire  $\text{UO}_2$ - $\text{ZrO}_2$  compositional range was experimentally investigated in the 1950's prior to this work [4,5]. More work was successively devoted to establish the main form of the  $\text{UO}_2$ - $\text{ZrO}_2$  phase diagram using conventional techniques at the same time [6].

While  $\text{UO}_2$  crystallizes in the cubic fluorite structure, pure  $\text{ZrO}_2$  has three polymorphic phases, monoclinic (at ambient conditions), tetragonal (at temperatures greater than 1440 K), and cubic of the fluorite structure (at temperatures above 2600 K). Meta-stable phases (tetragonal solid solution) have been identified by Piluso et al. [7] in the  $\text{UO}_2$ - $\text{ZrO}_2$  system.

Because of the strong correlation between the phase changes and the properties of  $\text{ZrO}_2$  [8–11], additional information can be extracted by studying the phase transformation reaction of  $\text{ZrO}_2$  at high temperature (e.g. during a nuclear accident), and at different corium  $\text{UO}_2/\text{ZrO}_2$  ratios.

In this work, samples of initially stoichiometric (U, Zr) $\text{O}_{2.00}$  across the full U/Zr compositional range were prepared using sol gel methods employed at the European Commission's Joint Research Centre of Karlsruhe (Germany). Such preparation approach gives similar structures as those obtained during a melt reaction in a reactor core. X-Ray Diffraction (XRD) was used here in order to follow the changes in the martensitic polymorphic transformation of both zirconium oxide and mixed uranium-zirconium oxides.

The melting behaviour of such samples was then analysed by laser heating coupled with fast optical spectro-pyrometry under a controlled atmosphere [12]. Such analysis constitutes a step forward with respect to the early melting point measurements reported by Wisnyi et al. [13] that were performed by more traditional furnace heating methods. In particular, the current approach permits studying the chemical environment effect on the material's melting behaviour. The latter was actually investigated here both under inert (pressurised Ar) and strongly oxidising (0.3 MPa air, i.e. 0.063 MPa  $\text{O}_2$ ) atmospheres. XRD, X-Ray Absorption Spectroscopy (XAS) and Scanning Electron Microscopy (SEM) were then used to characterise the samples and in particular to determine the uranium oxidation state in the materials melted and re-solidified under the different atmospheres. The oxygen potential for the hyperstoichiometric urania component was also calculated to have an insight on the thermodynamic behaviour of this system. The results were then compared with the phase boundaries optimised by a CALPHAD approach in the U-Zr-O system as reported by Chevalier et al. [14], Barrachin et al. [15], Piluso et al. [7], and Quaini [16].

The physico-chemical behaviour of the reactor core materials under severe accident conditions is capital for the mitigation and prevention of their consequences.

Main goals of the present analysis are thus a deeper understanding of the phenomena leading to the formation of corium in a LOCA, and new assessment of corium properties at temperatures near the solid-liquid transition.

## 2. Experimental

### 2.1. Sample preparation

A first batch of mixed oxide materials was prepared by a sol-gel assisted precipitation technique deployed at JRC Karlsruhe. Feed solutions with fixed  $\text{UO}_2/\text{ZrO}_2$  molar ratios of nominally 0/100, 20/80, 40/60, 50/50, 60/40, 80/20 and 100/0 were prepared from Zr-oxychloride and uranyl nitrate in distilled water. Following the addition of a surface-active agent and organic thickener, the solution was dispersed into droplets by a rotating cup atomizer. The droplets were collected in an ammonia bath, where spontaneous gelation occurs. After ageing, the resulting spheres were washed with distilled water and dried using an azeotropic distillation procedure with tetrachloroethylene. Due to varied rotating speed throughout the atomization the spheres have a polydisperse size distribution. Calcination under argon was carried out at 923 K. To obtain pellets the materials were pressed and sintered. Conventional pressing to pellets was obtained with a uni-axial press using a 7.1 mm matrix and a load of 15 kN. Sintering conditions were 6 h at 1923 K under  $\text{Ar}/\text{H}_2$ , with temperature ramps of 200 K/h for heating and cooling step on a Mo tray. These sintering conditions ensured the production of stoichiometric  $\text{UO}_2$ .

Another batch of mixed  $\text{UO}_2$ - $\text{ZrO}_2$  samples was prepared by a more straightforward powder metallurgy approach, in the aim of checking a possible influence of the sample synthesis method on the high temperature behaviour of these materials. This batch included samples with  $\text{UO}_2/\text{ZrO}_2$  molar ratios of nominally, 20/80, 45/55, 47.5/52.5, 70/30, 80/20, 85/15, 90/10 and 95/5. Powders of  $\text{UO}_2$  (from a sol-gel production) and commercially available  $\text{ZrO}_2$  were mixed together, and pressed to pellets with a uni-axial press (7.7 mm or 8.55 mm matrices with a load of 15–20 kN, 0.03% zinc stearate added as lubricant). These green pellets were sintered at 1873 K under  $\text{Ar}/\text{H}_2$  for several hours (with 200 K/h heating/cooling rate) in a metal furnace equipped with Mo crucibles/tray. Several of these pseudo-binary compositions have been investigated between  $x(\text{ZrO}_2) = 0.4$  and  $x(\text{ZrO}_2) = 1$ , in order to identify the minimum melting point in the system  $\text{UO}_2$ - $\text{ZrO}_2$ .

A first batch of mixed oxide materials were prepared by a sol-gel assisted precipitation technique deployed at JRC Karlsruhe. Feed solutions with determined  $\text{UO}_2/\text{ZrO}_2$  molar ratios of formally 0/100, 20/80, 40/60, 50/50, 60/40, 80/20 and 100/0 were prepared from Zr-oxychloride and uranyl nitrate in distilled water. Following the addition of a surface-active agent and organic thickener, the solution was dispersed into droplets by a rotating cup atomizer. The droplets were collected in an ammonia bath, where spontaneous gelation occurs. After ageing, the resulting spheres were washed with distilled water and dried using an azeotropic distillation procedure with tetrachloroethylene. Due to varied rotating speed throughout the atomization the spheres have a polydisperse size distribution. Calcination under argon was carried out at 923 K. To obtain pellets the materials were pressed and sintered. Conventional pressing to pellets was obtained with a uni-axial press using a 7.1 mm matrix and a load of 15 kN. Sintering conditions after pressing were 6 h at 1923 K under  $\text{Ar}/\text{H}_2$ , with temperature ramps of 200 K/h for both heating and cooling steps.

Another batch of mixed  $\text{UO}_2$ - $\text{ZrO}_2$  samples was prepared by a

more straightforward powder metallurgy approach, in the aim of checking a possible influence of the sample synthesis method on the high temperature behaviour of these materials. This batch included samples with  $\text{UO}_2/\text{ZrO}_2$  molar ratios of nominally: 20/80, 45/55, 47.5/52.5, 52.5/47.5, 70/30, 80/20, 85/15, 90/10 and 95/5. Several pseudo-binary compositions have been investigated between  $x(\text{ZrO}_2) = 0.4$  and  $x(\text{ZrO}_2) = 1$ , in order to identify the minimum melting point in the system  $\text{UO}_2\text{-ZrO}_2$ .

In both cases, pellets with a thickness of around 4 mm and a diameter of around 6 mm were used for the experiments.

## 2.2. Laser heating and temperature measurement

Details of the laser-heating setup used in this research have been reported in previous publications [12,17] although the technique has been partially improved in the present work.

Thermograms were measured by sub-millisecond resolution pyrometry on mixed  $\text{UO}_2\text{-ZrO}_2$  samples laser heated beyond melting by a TRUMPF® Nd:YAG cw laser radiating at 1064.5 nm. Its power vs. time profile is programmable with a resolution of 1 ms. Laser shots of different duration (from a few tens to a few hundreds ms) and laser power density ( $300 \text{ W cm}^{-2}$  to  $3000 \text{ W cm}^{-2}$ ) were repeated on the same 3-mm to 8-mm diameter spot on a single sample surface as well as on different samples of the same composition in order to obtain statistically significant datasets for each composition and heating cycle. With the current experimental parameters, a 10% - to 25% - mass fraction of the sample was typically melted and re-solidified, under self-crucible conditions. This corresponded to a few tens of mg of material, which was sufficient to be then further characterised by XRD, XAS and SEM.

During the shots, the investigated specimen was held in a sealed autoclave under controlled atmosphere. In a first series of experiments, the atmosphere was chosen on the basis of thermodynamic equilibrium calculations between the condensed phases and the vapour, in order to maintain as much as possible the original composition of each sample throughout the heating/cooling cycles. Thus  $\text{UO}_2$ -rich samples were mostly heated under an inert atmosphere (slightly pressurised argon at 0.3 MPa), whereas  $\text{ZrO}_2$ -rich ones were preferably studied under 0.063 MPa  $\text{O}_2$  at 0.3 MPa, in order to minimize oxygen losses from the condensed phases. Successively, laser heating tests were carried out under 0.063 MPa  $\text{O}_2$  on all the compositions, in order to study their high-temperature oxidation behaviour. In performing such experiments, it is reasonable to assume that an equilibrium oxygen-to-metal ratio would be reached very quickly in the condensed material during melting and solidification above 2500 K, thanks to the fast kinetics.

Thermal shock was minimised by applying a pre-heating level around 1500 K to limit thermal stresses due to the extreme laser power density impinging on the surface of the sample. The procedure consisted of heating the sample at that temperature before starting the actual high-power pulses. Also during the series of four heating-cooling cycles on the same sample spot the material was not allowed to cool below an intermediate temperature of approximately 1500 K. The duration of the high-power pulses was increased from one heating-cooling cycle to the other, in order to check the result repeatability under slightly different experimental conditions (Fig. 1). This approach ensured a better mechanical stability of the samples, over which several successive shots could be repeated to check the result reproducibility and the eventual effects of non-congruent vaporisation or segregation phenomena. The onset of melting was detected by the appearance of vibrations in the signal of a probe laser ( $\text{Ar}^+$  cw 750 mW to 1.5 W) reflected by the sample surface (Reflected Light Signal technique, or RLS) [12]. The sample cooled naturally when the laser beam was switched off during the thermal cycle. Thermal arrests corresponding to

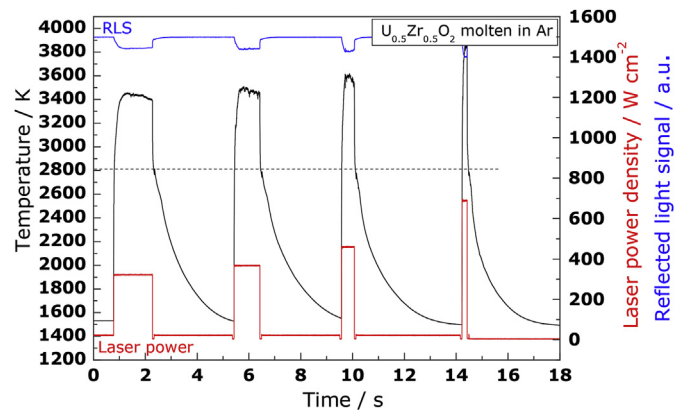


Fig. 1. Sequence of laser pulses performed on a  $\text{U}_{0.5}\text{Zr}_{0.5}\text{O}_2$  sample under Ar. The red plot gives the power profile of the laser beam impacting the surface of the sample. The black plot represents the temperature measured by the first channel of the pyrometer at 655 nm and the blue plot is the reflected light signal measured by the second channel at 488 nm. The dotted line indicates the average solidification temperature.

solidification were then observed on the thermograms recorded by the fast pyrometers. These operate in the visible-near infrared range between 488 nm and 900 nm. The reference pyrometer wavelength was here 655 nm. This was calibrated according to the procedure already reported elsewhere [12]. Direct measurement of the sample thermal emission yielded the radiance temperature at the pyrometer wavelength. The sample real temperature was obtained from the radiance temperature using the following pyrometry equation, which can be easily derived from Planck's radiation law corrected with the normal spectral emissivity  $\varepsilon_\lambda$ :

$$\frac{1}{T} = \frac{1}{T_\lambda} + \frac{\lambda}{c_2} \ln \varepsilon_\lambda(\lambda, T) \quad (1)$$

Equation (1) is valid within Wien's approximation to Planck's law, i.e. when  $\exp\left(\frac{c_2}{\lambda \cdot T}\right) > > 1$ .

If  $\lambda$  is expressed in  $\mu\text{m}$  and  $T$  in K, then the universal constant  $c_2$  takes the value of 14388  $\mu\text{m K}$ .

The normal spectral emissivities ( $\varepsilon_\lambda$  or NSEs) of urania and zirconia have been assumed to be equal to 0.83 and 0.9, respectively, as determined from previous work [12,20]. Values of intermediate compositions have been obtained by linearly interpolating the two end member values according to the volume fraction of each component. The latter was considered to provide the best estimate of the surface fraction averaged over all the possible grain orientations. These NSE values have been cross-checked in the current work with the help of a multi-wavelength spectro-pyrometer. This approach, similar to the one reported in Ref. [12], consists in the measurement during the current heating cycles of the thermal emission (or radiance) spectra of the sample. Non-linear minimum-square fit of such spectra, using Planck's equation corrected for the normal spectral emissivity, yield values for real temperature and NSE throughout the heating/cooling cycles, although with a more limited time resolution than the above mentioned single-channel pyrometer.

Uncertainty of the measurements was calculated according to the error propagation law [12], taking into account the uncertainty associated with pyrometer calibration, emissivity, transmittance of the optical system and the accuracy in detecting the onset of vibrations in the RLS signal. The estimated cumulative uncertainty is thus  $\pm 1\%$  of the reported temperatures in the worst cases, with a 1- $k$  coverage factor (corresponding to one standard deviation around the average value).

### 2.3. XRD analysis

The structure of the materials was determined at room temperature by X-Ray diffraction using a Bruker D8 X-ray diffractometer mounted in a Bragg–Brentano configuration with a curved Ge monochromator (1,1,1), a copper tube (40 kV, 40 mA) equipped with a LinxEye position sensitive detector. For the measurement, the ground powders were deposited on a silicon wafer to minimize the background and dispersed on the surface with 2 or 3 drops of isopropanol. Structural analyses were performed with the JANA 2006 software suite [21] by the Le Bail method. Only the profile fitting is used with predefined phases, resp. mixture of phases as no additional unknown phases were obtained.

### 2.4. X-ray absorption spectroscopy

X-ray Absorption Near Edge Structure (XANES) and Extended X-ray Absorption Fine Structure (EXAFS) measurements were performed at the Rössendorf Beamline (RÖBL, Beamline 20) of the European Synchrotron Radiation facility (ESRF, Grenoble). Only XANES results are presented in this work. Measurements were performed on small amounts (5 mg) of powdered samples mixed with boron nitride (BN) and pressed into pellets. XANES spectra were collected at room temperature in the transmission and fluorescence mode at the Zr K and U  $L_{III}$  edges. Energy calibration was achieved by measuring the K XANES spectrum of a Y reference foil (17038 eV) located between the second and third ionization chambers. The XANES spectra have been normalized using linear functions for pre- and post-edge modelling. The white-line maxima have been taken as the first zero-crossing of the first derivative. Pre-edge removal, normalization and self-absorption correction were performed using the ATHENA software [22]. The XANES spectra edges were compared to those of reference samples, i.e.  $UO_2$ ,  $U_3O_8$ ,  $U_4O_9$  and  $UO_3$ . The U oxidation state was determined using a linear combination fitting of the reference spectra.

### 2.5. Scanning electron microscopy

Philips XL40 scanning electron microscope (SEM) operated at 20 kV and installed in a glove box was employed in the present research. Quantitative Energy Dispersion Spectrometry (EDS) analysis and X-ray element maps were acquired, using a shielded Cameca SX100R electron microprobe.

## 3. Results

### 3.1. Melting temperatures

Typical thermograms recorded during the current heating cycles are reported in Figs. 1 and 2. Pure end members ( $UO_2$  and  $ZrO_2$ ) were initially measured in such a way as to preserve as much as possible the original oxygen-to-metal stoichiometry (2.00). Therefore uranium was melted under pressurised argon, and zirconia under 0.063 MPa  $O_2$ , yielding solid-liquid transitions at  $3120\text{ K} \pm 30\text{ K}$  and  $2970\text{ K} \pm 30\text{ K}$ , respectively. The mixed oxides and pure  $UO_2$  were successively measured under both atmospheric conditions to cover also scenarios that include oxygen ingress into the core vessel.

Fig. 1 shows typical thermograms resulting from a melting point measurement under pressurised argon at 0.2 MPa on a ( $U_{0.5}Zr_{0.5}$ )  $O_2$  sample prepared by the sol-gel assisted precipitation. At the beginning of a laser pulse, the sample surface temperature recorded by the 655 nm pyrometer increases very rapidly due to the contribution of thermal radiation emitted by the hot surface. After the end of the laser pulse, the temperature decreases rapidly, the

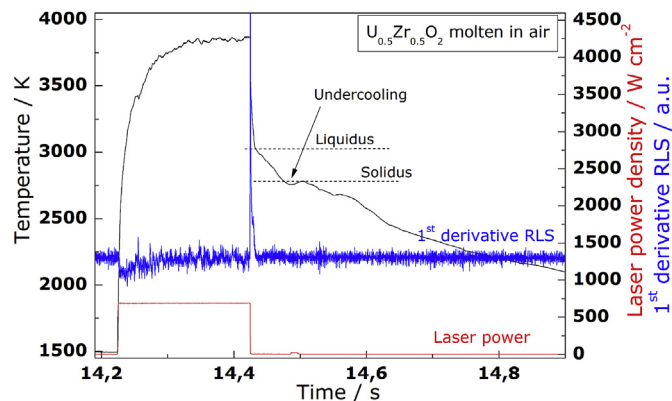


Fig. 2. Example of a melting/solidification measurement on  $U_{0.5}Zr_{0.5}O_2$  in air.

sample surface cools and a freezing thermal arrest is visible in the thermogram at a temperature corresponding to the dotted line in Fig. 1. As expected, no inflection in the heating flank is visible since thermal equilibrium conditions were not achieved in this part of the measurement, where the laser delivers a large amount of heat in a short time interval on the sample surface [23].

Therefore, the reflected light signal (RLS) at 488 nm constitutes a significant mean for identifying the phase transformation when it is not evident in the thermogram. The melting point as well as the solidification point can be identified as a sudden variation in the reflected light signal. When an extremely thin, motionless molten layer is formed, it reflects a part of the Ar laser beam into the pyrometer detector. The RLS oscillates after the formation of the liquid mass that vibrates under capillarity forces, and correspondingly scatters the incident laser beam. The angular reflectivity of the sample changes during the stage of heating with the first appearance of liquid leading to a variation in the RLS. When the surface solidifies again the oscillations of the liquid mass stop and the RLS vibrations disappear.

Depending on the amount of liquid formed during heating, the resulting freezing thermal arrest is more or less pronounced on the cooling flank, but no significant influence of the laser pulse duration and intensity is observed on the behaviour of the sample during cooling. In general, for samples heated in an inert or reducing atmosphere, the measured solidification temperatures are reproducible for all the sequences of the laser pulse as in Fig. 1. An average solidification temperature was obtained here with a low uncertainty (cf. section 2.2), mostly due to the standard deviation of experimental points and the uncertainty of the pyrometer reading, as indicated in the previous section. The observed repeatability of the solidification temperature implies that the cooling rate hardly affects the solidification points, confirming that in inert gas the current thermal analysis is performed under local thermodynamic equilibrium conditions. Table 1 gives the values for the solidification temperatures obtained for the different compositions in inert atmosphere (argon).

A magnification of a laser pulse of a sequence performed in air on the sample  $U_{0.5}Zr_{0.5}O_2$  is shown in Fig. 2.

When melted in an oxidising (0.063 MPa  $O_2$ ) atmosphere, significant differences were noticed between thermal arrests recorded for uranium-rich compositions compared to the arrests in an inert (argon) atmosphere. This behaviour shows that significant oxidation occurs during the shots performed in 0.063 MPa  $O_2$ , as will be detailed in the following sections. In Fig. 2 it can be seen that, for the sample melted in oxidising conditions, the liquid/solid transition occurs in two steps, unlike the same experiments carried out under pressurised argon: a liquidus point, corresponding to the

**Table 1**  
Solidification points determined by laser heating for the various ZrO<sub>2</sub>-UO<sub>2</sub> compositions under inert and oxidising atmosphere.

Sample	Inert atmosphere (Ar)				Oxidising atmosphere (air)			
	Liquidus/K	Uncertainty/K	Solidus T/K	Uncertainty/K	Liquidus T/K	Uncertainty/K	Solidus T/K	Uncertainty/K
UO <sub>2</sub>	–	–	3120	32	–	–	2585	39
U <sub>0.8</sub> Zr <sub>0.2</sub> O <sub>2</sub> <sup>a</sup>	3045	15	2981	24	–	–	2567	37
U <sub>0.6</sub> Zr <sub>0.4</sub> O <sub>2</sub>	–	–	2841	28	2795	138	2493	34
U <sub>0.5</sub> Zr <sub>0.5</sub> O <sub>2</sub>	–	–	2788	18	2916	56	2621	60
U <sub>0.475</sub> Zr <sub>0.525</sub> O <sub>2</sub> <sup>a</sup>	–	–	2820	28	2990	80	2698	23
U <sub>0.45</sub> Zr <sub>0.55</sub> O <sub>2</sub> <sup>a</sup>	–	–	2815	28	–	–	–	–
U <sub>0.4</sub> Zr <sub>0.6</sub> O <sub>2</sub>	–	–	2796	10	2787	20	2607	49
U <sub>0.3</sub> Zr <sub>0.7</sub> O <sub>2</sub> <sup>a</sup>	–	–	2806	10	–	–	2770	20
U <sub>0.2</sub> Zr <sub>0.8</sub> O <sub>2</sub>	–	–	2811	10	–	–	2747	21
U <sub>0.2</sub> Zr <sub>0.8</sub> O <sub>2</sub> <sup>a</sup>	–	–	2829	10	2877	40	2773	20
U <sub>0.15</sub> Zr <sub>0.85</sub> O <sub>2</sub> <sup>a</sup>	–	–	2853	10	–	–	2840	10
U <sub>0.1</sub> Zr <sub>0.9</sub> O <sub>2</sub> <sup>a</sup>	–	–	2885	10	–	–	2865	22
U <sub>0.05</sub> Zr <sub>0.95</sub> O <sub>2</sub> <sup>a</sup>	–	–	2919	30	–	–	2888	9
ZrO <sub>2</sub>	–	–	2970	30	–	–	2970	30

<sup>a</sup> Samples were prepared with the powder metallurgy approach.

formation of the first solid seeds in the liquid mass, and a solidus point, corresponding to total solidification of the sample surface. It can also be appreciated, that total solidification occurs here at a lower temperature compared to the same test performed in pressurised argon.

Fig. 2 also shows the usefulness of the RLS technique on such samples. Thanks to this technique it was possible to estimate the time interval during which there was a liquid phase on the sample surface and therefore one could determine the melting point on the heating flank of a thermogram.

Also the undesirable effect of undercooling can be observed. The cooling rate was so rapid that the liquid was initially cooled below the freezing point (undercooling). The solidification started at the bottom of the molten pool on the specimen surface where the liquid was in contact with the unmolten solid surface. Then while the solid edge kept growing, the temperature started to rise up to a local maximum due to the release of latent heat of solidification. This maximum temperature corresponded to the formation of a completely re-solidified layer at the surface of the sample. The release of the latent heat of solidification from the remaining molten material enclosed under the surface crust counteracted the process of cooling of the solid surface, itself driven by radiation and convection/conduction. A second slight inflection after the local maximum occurred at lower temperature. As proven by existing thermo-mechanical modelling of similar experiments [23], this second inflection corresponded to total solidification of the last inner liquid mass. After the last inflection the solidified sample continued cooling to ambient temperature. Looking at the thermogram in Fig. 2 two thermal arrests on the cooling flank are noticeable. The pyrometer allowed the detection of the first solid phase formed at 14.42 s and the complete solidification of the sample at around 14.55 s, corresponding to the first and the second thermal arrests, where the RLS also showed changes.

Table 1 summarises the average solidus and liquidus temperatures obtained in laser heating experiments of the whole set of samples prepared with the two techniques presented in section 2.1, for both atmospheric conditions used (pressurised argon and air). As explained in section 2.1, two samples with UO<sub>2</sub>/ZrO<sub>2</sub> molar ratio respectively 20/80 and 80/20 were prepared with both techniques for checking the influence of the synthesis method. Unfortunately, a direct comparison could only be made between the solidification points obtained in argon in the U<sub>0.2</sub>Zr<sub>0.8</sub>O<sub>2</sub> samples, as both the U<sub>0.8</sub>Zr<sub>0.2</sub>O<sub>2</sub> and U<sub>0.2</sub>Zr<sub>0.8</sub>O<sub>2</sub> samples synthesised by sol-gel assisted precipitation were shattered when laser-heated in air. As reported in Table 1, the two U<sub>0.2</sub>Zr<sub>0.8</sub>O<sub>2</sub> samples show similar solidification

temperatures in argon within the experimental uncertainty. Other compositions prepared with the two different approaches display a similar solidification point trend, confirming the independence of the melting behaviour on the synthesis method.

When the results obtained on all samples are considered together, one can observe that solidification points recorded in argon follow a rather regular evolution across the investigated compositional range. However, in Zr-rich samples, initially having a light grey appearance, the material melted in argon became black or dark-grey, most probably due to the creation of oxygen defects after melting at high temperature [18]. In mixed compositions, the melting/freezing temperatures decrease from those of pure UO<sub>2</sub> and ZrO<sub>2</sub> to reach a minimum slightly below 2800 K between U<sub>0.5</sub>Zr<sub>0.5</sub>O<sub>2</sub> and U<sub>0.3</sub>Zr<sub>0.7</sub>O<sub>2</sub>. The solid/liquid equilibrium line is rather flat for a broad compositional range around this minimum in the UO<sub>2</sub>-ZrO<sub>2</sub> pseudo-binary plane. In this range, solidus and liquidus lines are very close, and could not be resolved with the current approach. In U-richer compositions, the solidus and liquidus are further apart, and were clearly distinguishable in the current laser heating experiments performed on U<sub>0.8</sub>Zr<sub>0.2</sub>O<sub>2</sub>.

Lower melting/freezing temperatures were observed when experiments were carried out in oxidising atmosphere and uranium-richer samples, as it can be remarked in Table 1. Under these conditions, solidification temperatures for Zr-rich compositions with  $x(\text{ZrO}_2) > 0.8$  were still similar to those recorded in inert gas. For all the investigated compositions, freezing thermal arrests measured in air were also more dispersed compared to those performed under Ar. In uranium-rich compositions, an evolution of the solidus temperature was observed over successive pulses in 0.063 MPa O<sub>2</sub>. In these cases, due to the high-temperature reactivity of uranium dioxide in the presence of oxygen, the sample surface underwent an oxidation reaction with the atmosphere during the laser shots, and only the final solidus temperature, approximately stabilised in the last pulses, is reported in Table 1.

Consequences of this kind of behaviour have been further investigated in the next samples characterisation section.

### 3.2. Sample characterisation

#### 3.2.1. X-ray diffraction

XRD bulk analysis was performed to investigate effects of the laser heating-melting treatment on the laser-irradiated material. The starting materials (sintered pellets with assumed stoichiometric composition U<sub>1-x</sub>Zr<sub>x</sub>O<sub>2.00</sub>) showed (metastable) cubic and tetragonal phases for all compositions except the high uranium

content material  $U_{0.8}Zr_{0.2}O_2$ , which only showed a cubic phase. This phase composition assessed for the starting materials is reasonably consistent with the phase diagram reported later in Fig. 6. The lattice parameters were also comparable to the cubic and tetragonal series published by Piluso et al. [7], pointing to a two phase starting material with a U-rich cubic phase and a Zr-rich tetragonal phase. The compositions of these two phases calculated from the Vegard's law obtained by Piluso were in the range  $U_{0.74}Zr_{0.26}O_2$  to  $U_{0.79}Zr_{0.21}O_2$  for the U-rich cubic phase and around  $U_{0.15}Zr_{0.85}O_2$  for the tetragonal Zr-rich phase.

The analysis on the molten and resolidified material was only possible by separating the laser-melted surface spot from the bulk pellet. This was a difficult operation and it was not always possible to precisely separate the melted from the unmelted material. Therefore, XRD measurements were performed on specimen possibly containing unmelted material, although the melted/resolidified part was in excess. An example of resulting diffractogram is shown in Fig. 3. Fig. 3 shows the diffractograms for the composition  $U_{0.5}Zr_{0.5}O_2$  before (a) (sintered starting material) and after (b) melting in argon.

The evaluation showed that the diffractogram for the starting material (given in red) could be reasonably fitted with three phases, two cubic ones (red triangles) and a tetragonal one (red bar). For all phases a correlation to the composition could be drawn assuming a stoichiometric material and Vegard's law for fcc and tetragonal phases, as established by Piluso et al. [7].

The material molten under argon (given in black) in this case indeed showed a significant amount of the starting material. Although the main phase observed was a tetragonal phase with lattice parameters that were not comparable to the high Zr-content material described by Piluso et al. [7], it showed a different a/c ratio. Such phase was also observed for other samples in the composition range  $U_{0.4}Zr_{0.6}O_2$  to  $U_{0.6}Zr_{0.4}O_2$ . As no significant volatilisation of U-oxides could be reasonably assumed under the applied melting conditions, one could tend to assume here a slight segregation, upon cooling, of metastable tetragonal (U, Zr) mixed oxide phases in a composition range  $U_{0.4}Zr_{0.6}O_2$  to  $U_{0.6}Zr_{0.4}O_2$ , within an unchanged overall composition. Anyhow, such U-rich tetragonal phase is not necessarily expected to exist when considering the actually established U-Zr-O phase diagram [2,3,16], its appearance may be due to the fast quenching the samples had undergone after the laser pulses.

When melting in air a phase change into a face-centred-cubic (fcc) phase (or possibly two phases taking into account the very asymmetric peak shapes) was observed as reported in Table 2. Beside this fcc phase only minor diffraction peaks were observed that may be correlated to higher U-oxide ( $U_4O_9$ ,  $U_3O_8$ ) or mixed oxide phases ( $ZrU_2O_7$ ). Due to the low intensities of these peaks a final assignment was not possible. In this case residues of the unmolten material were not observed in significant amounts.

For all investigated samples and atmospheric conditions the obtained molten materials show a variety of cubic and tetragonal and, for high Zr-contents, also monoclinic phases. These should not be interpreted as thermodynamically stable compounds but as metastable phases that are formed most probably as a result of the fast cooling.

The data shown in Table 2 reveal a trend depending on the composition and the melting atmospheres.

In samples melted and quenched under argon, tetragonal phases prevailed for all compositions investigated ( $U_{0.5}Zr_{0.5}O_2$  to  $U_{0.2}Zr_{0.8}O_2$ ). These phases seemed to retain the original nominal composition. They most probably did form due to the fast quenching of the samples and were considered to be metastable.

In samples melted and quenched under air, the obtained phases were preferably cubic except for the high Zr-content sample, in which tetragonal and monoclinic phases were clearly observed. The cubic phases show distinctly smaller lattice parameters than the ones found in the as-sintered materials. This would mean either that the U-content of the samples is strongly reduced or that the uranium is oxidised to higher valence states. Both possibilities would lead to a decrease of the lattice parameter in the cubic system [23]. For example, one can refer to the lattice parameter decrease for cubic mixed (U, Zr)-oxides mentioned by Piluso et al. [7],  $a = 5.468 + 0.3296x \text{ \AA}$  or the difference between the lattice parameter of  $UO_2$  ( $a = 5.47 \text{ \AA}$ ) compared to the cubic  $U_4O_9$  with a lattice parameter around  $5.44 \text{ \AA}$  [23]. Although the crystallographic changes an oxidation process in the cubic mixed (U, Zr)-oxide could not be quantified in detail from the available diffractograms the oxidation seemed the most reasonable explanation of the XRD results considering XANES results discussed in the next section 3.2.2. Possible vapourisation losses of higher U-oxides during the melting process cannot be excluded completely, but they are unlikely under the applied melting conditions under pressurised gas. Moreover, no relevant uranium losses were detected in the present SEM-EDX

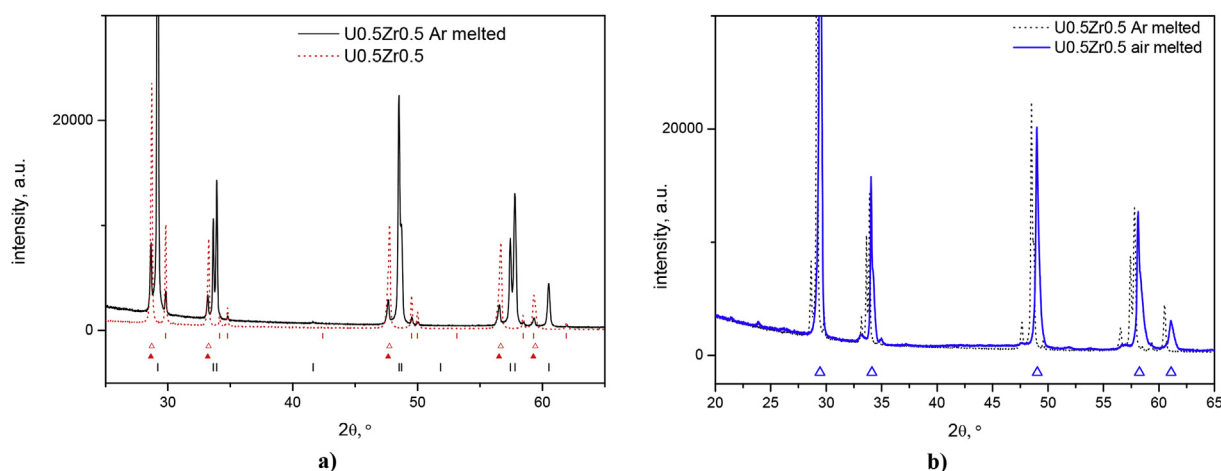


**Fig. 3.** X-ray diffractograms of  $U_{0.5}Zr_{0.5}O_2$ . (a): sintered starting material compared to Argon molten material. Red, dotted diffractogram: as sintered fitted with 2 fcc phases (red triangles) and a tetragonal phase (red bars). Black diffractogram: melted in Ar fitted with a tetragonal phase (black bars + residues of the unmelted material not shown) (b): melted samples in air and in Ar. Black, dotted diffractogram: melted in Ar. Blue diffractogram: melted in air fitted with a fcc phase (blue triangles) more phases are present, but further fitting was not successful.

**Table 2**  
Lattice parameters and phase assignment of the  $\text{UO}_2\text{-ZrO}_2$  various compositions of unmelted and re-solidified material.

Composition	Lattice parameters/Å										
	a = b or a = b = c	c	phase	a = b or a = b = c	c	phase	a = b or a = b = c	b	c	$\beta$	phase
	Sintered			melted in Ar			melted in air				
$\text{U}_{0.8}\text{Zr}_{0.2}\text{O}_2$	5.400		fcc	n.d.			5.350				fcc1
$\text{U}_{0.6}\text{Zr}_{0.4}\text{O}_2$	5.385		fcc1	n.d.			5.397				fcc2
	5.398		fcc2				5.287				fcc1
	3.647	5.250	tet				5.290				fcc2
$\text{U}_{0.5}\text{Zr}_{0.5}\text{O}_2$	5.383		fcc1	3.735	5.324	tet	5.249				fcc
	5.395		fcc2								
	3.648	5.250	tet								
$\text{U}_{0.4}\text{Zr}_{0.6}\text{O}_2$	5.400		fcc1	3.73	5.321	tet	5.244				fcc
	5.383		fcc2								
	3.646	5.250	tet								
$\text{U}_{0.2}\text{Zr}_{0.8}\text{O}_2$	5.385		fcc	5.395		fcc	3.639	3.639	5.238		tet
	3.649	5.253	tet	3.659	5.257	tet	5.194	5.229	5.360	97.91	mon

Starting material residues possibly seen in the molten material's XRD are not considered as separate phases in this table.

n.d. samples did not give usable molten parts.

The uncertainty for the determination of the lattice parameters is not better than  $\pm 0.001$  Å.

analyses on the melted samples.

### 3.2.2. XAS analysis

In the current materials, uranium can exist in the (IV) oxidation states in the ideal, defect-free dioxide. However, a disproportion can occur by which uranium tends to be oxidised to the (V) and (VI) oxidation states and, potentially, reduced to U(III). This allows the formation of both hypo-stoichiometric (with mostly U (III) and U (IV)) and hyper-stoichiometric dioxides (with mostly U (IV), U (V) and U (VI)). An oxidising atmosphere results in the oxidation of uranium dioxide to  $\text{UO}_{2+x}$  or even to higher oxides, such as  $\text{U}_4\text{O}_9$ ,  $\text{U}_3\text{O}_8$  and  $\text{UO}_3$  [23]. Zr instead, that is known to exist only in the (III) and (IV) oxidation states in the oxide forms, was observed to be stable at a composition very close to stoichiometry,  $\text{ZrO}_{2.00}$ .

Thus, an important point in the interpretation of the melting behaviour of oxide systems containing  $\text{UO}_2$  is the possible change of the oxidation state of uranium under oxidising atmosphere. XANES experiments were performed at the RÖBL line of the ESRF synchrotron in order to investigate the oxygen behaviour both in fresh and laser-heated samples. XANES results, presented in Table 3 and Fig. 4, quantify the oxidising effect of laser heating under 0.063 MPa  $\text{O}_2$ , in terms of oxygen/metal ratio.

Fig. 4 shows example XANES spectra recorded on  $\text{U}_{0.6}\text{Zr}_{0.4}\text{O}_{2+y}$  as fabricated and after melting in pressurised air. Spectra, fitted using ATHENA<sup>TD</sup>, are compared with the  $\text{U L}_{III}$  absorption edges measured on  $\text{UO}_2$ ,  $\text{U}_4\text{O}_9$  and  $\text{U}_3\text{O}_8$ , taken as references as 100% U(IV), 50% U(IV) + 50% U(V), 33% U (V) + 67% U (VI), respectively. The white line energy ( $E_{\text{WL}}$ ) position, the most intense absorption resonance for the  $\text{L}_{III}$  edge of tetravalent uranium in  $\text{UO}_2$  is represented as a dashed line. Assuming these latter reference lines, the XANES spectrum of the current sample is deconvoluted according to the following equation:

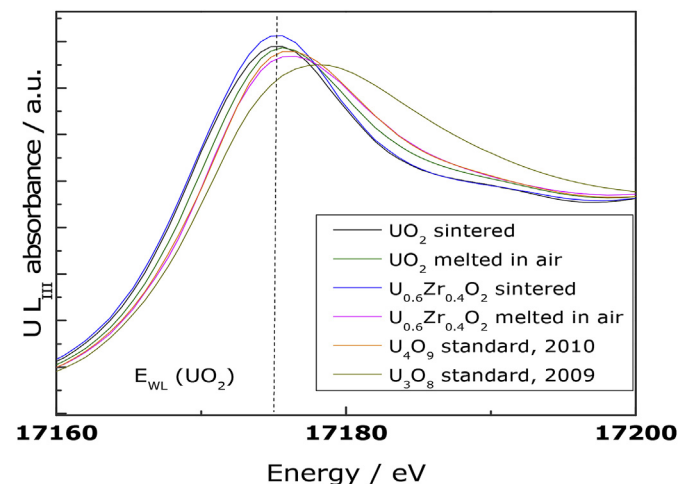


**Fig. 4.**  $\text{U L}_{III}$  XANES spectra collected at ESRF on a sample of  $\text{U}_{0.6}\text{Zr}_{0.4}\text{O}_2$  both melted and sintered and on some reference compounds.

$$S_C = aS_{\text{UO}_2} + bS_{\text{U}_4\text{O}_9} + cS_{\text{U}_3\text{O}_8} \quad (2)$$

In equation (2),  $S_C$  is the absorption near-edge spectrum of the current sample.  $a$ ,  $b$  and  $c$  represent respectively the fractions of the U(V), 0.5 (U(IV)+U(V)) and 0.33 U(V)+0.67 U(VI) contributions to the spectral fit. The  $a$ ,  $b$  and  $c$  fractions yielding the best spectral fit can be rearranged in order to obtain the total contents of U(IV), U(V) and U(VI) in the sample under analysis. In this way, one can determine an average uranium valence, which, divided by 2 (the valence of oxygen cations), yields the average oxygen-to-metal (O/

**Table 3**  
XANES results and Oxygen/Metal ratio obtained for  $\text{UO}_2\text{-ZrO}_2$  samples melted in 0.063 MPa  $\text{O}_2$ .

	$\text{UO}_2\%$	$\text{U}_4\text{O}_9\%$	$\text{U}_3\text{O}_8\%$	U (IV) %	U (V) %	U (VI) %	O/U	O/M
$\text{UO}_2$	40.5	57.2	2.3	69.10	30.13	0.77	$2.16 \pm 0.01$	$2.16 \pm 0.01$
$\text{U}_{0.6}\text{Zr}_{0.4}\text{O}_2$	33	54	13	60.00	35.67	4.33	$2.22 \pm 0.01$	$2.13 \pm 0.01$
$\text{U}_{0.5}\text{Zr}_{0.5}\text{O}_2$	40.7	45.4	13.9	63.40	31.97	4.63	$2.21 \pm 0.01$	$2.10 \pm 0.01$
$\text{U}_{0.2}\text{Zr}_{0.8}\text{O}_2$		99.7	0.3	47.85	51.38	0.77	$2.25 \pm 0.01$	$2.06 \pm 0.01$

Standard uncertainty: molar fraction = 1% and O/U and O/M = 0.01.

Zr was observed to always remain the oxidation state (IV).

M) ratio in the analysed sample. Since zirconium was observed to exist, in the current solid solutions, almost only as Zr (IV) the oxygen-to-zirconium molar ratio can be fixed, with good accuracy, at  $O/Zr = 2.00$ . Hence, the oxygen-to-uranium ratio  $O/U$  can be obtained in the investigated samples. This latter ratio is important for thermodynamic considerations on the oxygen potential that will be discussed in the following section. The significant steps of these procedure and the final  $O/M$  and  $O/U$  results are reported in Table 3. The experimental uncertainty of these results has been conservatively assessed to be  $\pm 0.01$  on the  $O/M$  ratio.

Due to the limited amount of melted material and the difficulty in separating it from the unmelted sample, XANES analysis could be successfully applied only to four of the current compositions melted and quenched in air. Nonetheless, a consistent shift of the experimental  $O/M$  towards higher values with increasing U content in the samples is quite evident from the current data, whereas the  $O/M$  of unmelted samples was in all cases 2.00 within the experimental uncertainty.

The present XANES results combined to the XRD and SEM analyses, assign actual  $U/Zr$  and  $O/(U + Zr)$  compositions to the final solidification temperature data.

### 3.2.3. Scanning electron microscopy

The laser melted sample surfaces were also analysed with scanning electron microscopy at different magnifications. An example of such analysis can be seen in Fig. 5a, where the re-solidified surface of an  $U_{0.5}Zr_{0.5}O_2$  sample is shown. In the back-scattered electrons (BSE) image Fig. 5b only a homogeneous material distribution on the surface was found. No relevant changes in composition were detected by Energy-dispersive X-ray (EDX) analysis along the surface between re-solidified and unmelted material. However, with the magnification used in this analysis method small differences were difficult to determine. In addition, SEM-EDX analysis provides only a semi-quantitative elemental composition of a material spot, so different phases having similar composition were not observable.

## 4. Discussion

Combining the current quasi-containerless laser heating method with further material characterisation, new results have been obtained concerning the liquid/solid transition in the U-Zr-O systems under inert and strongly oxidising conditions. The material characterisation performed before and after melting by SEM, XRD and XAS has allowed, in many cases, to identify and explain phase separation and oxidation phenomena occurring during the

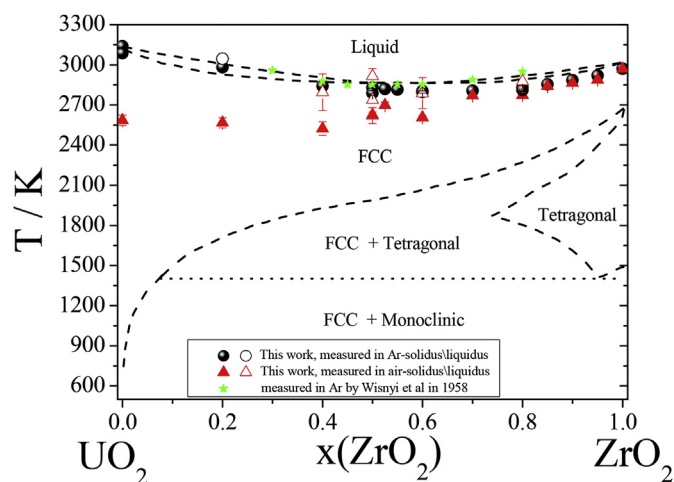


Fig. 6. The pseudo-binary  $UO_2$ - $ZrO_2$  phase diagram. (a) CALPHAD optimised phase boundaries based on the NUCLEA database ([11,12]) are plotted along with the current and previous experimental points. The melting points measured in argon lie on the optimised phase boundaries (dotted lines) while the points measured in 0.063 MPa  $O_2$  lie approximately between  $ZrO_2$  and  $UO_{2.16}$ .

liquefaction/solidification processes.

Results obtained in argon suggest that a minimum melting point exists in the pseudo-binary  $UO_2$ - $ZrO_2$  system, at a composition near to  $U_{0.4}Zr_{0.6}O_2$  and a temperature close to 2800 K. In contrast, experimental data recorded in the oxidising atmosphere are more complex. From the data obtained in 0.063 MPa of  $O_2$ , it is possible to propose a minimum melting point at a temperature close to 2500 K and at a composition near to  $U_{0.6}Zr_{0.4}O_2$ . These results are useful for the simulation of an accident environment where the fuel, hyperstoichiometric in oxygen, interacts with oxidised Zircaloy (i.e.  $ZrO_2$ ) and may melt up to 300 K below the melting point of the same composition in an inert atmosphere. Fig. 6 shows the solidus-liquidus data points obtained in this work, plotted against the pseudo-binary  $UO_2$ - $ZrO_2$  plane of the ternary U-Zr-O phase diagram.

The data points obtained in this work can be additionally compared with phase boundaries defined by CALPHAD optimisation in the U-Zr-O system [14–16]. It is obvious that only experimental points measured in argon agree with the CALPHAD optimised phase boundaries (dotted lines) in the whole pseudo-binary diagram. Only for Zr-rich compositions, the solidification points measured in air agree well with CALPHAD-assessed values in

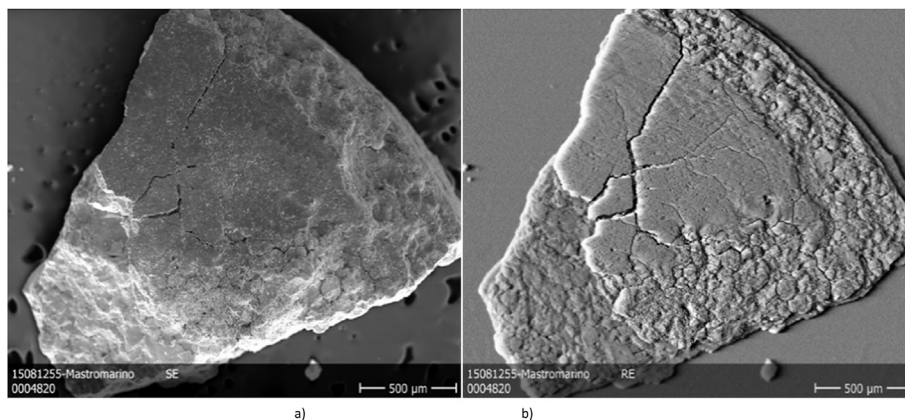


Fig. 5. Post-melting (a) Secondary Electron image and (b) Back Scattered Electron images of  $U_{0.5}Zr_{0.5}O_2$ .

the pseudo-binary plane.

The expected oxidising effect of laser heating under compressed air can be confirmed by the current XANES analysis data in terms of oxygen/metal ratio reported in Table 3. The lower solidus points recorded in pressurised air correspond to compositions largely enriched in oxygen. In fact it was clearly shown also in previous research [25–27], that hyper-stoichiometric uranium dioxide melts at a much lower temperature than the stoichiometric  $\text{UO}_{2.00}$  dioxide. Considering the experimental uncertainty on the O/U ratio ( $\pm 0.01$ ), the solidus temperature observed in this work for pure hyper-stoichiometric uranium dioxide ( $\text{UO}_{2.16}$ ) is in fairly good agreement with the data measured by Manara et al., in 2005 [26] and further assessed by Guéneau et al. [27]. The solidus temperature depression is very relevant starting for compositions with  $x(\text{UO}_{2+z}) \geq 0.5$  and can reach almost 650 K. Fig. 7 shows the evolution of the solidus/liquidus temperatures for the various compositions in the different atmospheric conditions. The present results show that a strongly oxidising atmosphere has an effect on the solidus temperature also in mixed uranium-zirconium dioxides, despite the stabilising effect that Zr (III, IV) produces on the chemical stability of the solid dioxide. This particular point can be better explained by calculating the oxygen potential corresponding to the various O/U ratios obtained with the XANES analysis and reported in Table 3.

The oxygen potential of actinide dioxides plays a crucial role in the high temperature behaviour of these compounds [24]. It is defined as:

$$\mu_{\text{O}_2} = RT \ln(p^*(\text{O}_2)) \quad (3)$$

where  $R$  is the ideal gas constant,  $T$  the absolute temperature and  $p^*(\text{O}_2)$ , the oxygen partial pressure referred to the standard atmospheric pressure (101325 Pa). This parameter defines the tendency for a compound to exchange oxygen with its environment. In particular, it plays a fundamental role in defining the high-temperature equilibrium of uranium dioxide as a pure, non-stoichiometric compound or mixed with other dioxides. The oxygen potential at 0.3 MPa of air, or 0.063 MPa  $\text{O}_2$ , at the solidus melting temperatures reported in this work, was calculated

through Equation (3) to be  $-10000 \pm 500 \text{ J mol}^{-1}$ , considering 0.10 MPa  $\text{O}_2$  as the reference state for oxygen. The oxygen potentials for pure urania and the urania-zirconia specimens were calculated in some compositions for which the oxygen potential versus O/U ratio was assessed in the thermodynamic model proposed by Lindemer and Besmann [28]:

$$RT \ln(p(\text{O}_2)) = -312800 + 126 T + 2 RT \ln(z(1-2z)^2 / (1-3z)^3) \quad (4)$$

This equation adequately represents all known data for  $\text{UO}_{2\pm z}$  oxygen potential dependence on uranium dioxide hyper-stoichiometry  $z$ . The oxygen potential results are presented in Table 4 for the composition analysed here by XANES.

For pure uranium dioxide melted in compressed air, a value  $\text{O}/\text{U} = 2.16$  is obtained (hyperstoichiometry  $z = 0.16$ ). The corresponding oxygen potential at the reported solidus temperature of 2585 K is  $-14700 \text{ J/mole}$ , and at  $z = 0.166$  it agrees, within the uncertainty of 0.01 for the experimental O/U, with the  $-10000 \text{ J/mol}$  of the air atmosphere. It can be concluded that the experimental results agree fairly well with Lindemer and Besmann's thermodynamic representation of pure hyperstoichiometric urania. Hence, it can also be concluded that the O/U ratio at the solidification point is reasonably preserved during quenching to ambient temperature, at least within the resolution limits of the current material characterisation techniques. Extrapolating this conclusion to mixed hyperstoichiometric urania-stoichiometric zirconia compositions, one can infer that increasing the zirconia content has the effect of stabilising increasingly higher O/U values at the experimental oxygen potential  $\mu_{\text{O}_2} = -10000 \text{ J mol}^{-1}$ , which is much lower than the oxygen potential expected for the same O/U ratios in pure urania reported in Table 4. Therefore, the total stabilisation effect for the zirconia-containing samples, reported in the fourth column of Table 4, is energetically quantified by adding  $\mu_{\text{O}_2}$  ( $10000 \pm 500 \text{ J mol}^{-1}$ ) to the values shown in the third column of Table 4. The total stabilisation effect includes the ideal-solution term  $RT \cdot \sum_i x_i \ln x_i$ , which is also reported in the fifth column of Table 4. The difference between the absolute values of the total stabilisation effect and the ideal-solution term yields the energetic decrease of the oxygen potential chemically ascribable to the presence of  $\text{ZrO}_2$  in the mixture (last column of Table 4). The oxygen potential values are typically affected by a quite large,  $\pm 10000 \text{ J mol}^{-1}$ , average uncertainty. This value has been obtained by combining, based on the independent error propagation law [12], single uncertainties of  $z$  and  $T$  values. These energetic values should therefore be considered as best estimates only. They will nonetheless be useful for further CALPHAD assessment of the U-Zr-O system.

One may also notice in Figs. 6, and 7 that at 0.5 mol fraction of zirconia, the liquidus temperature in 0.063 MPa  $\text{O}_2$  is comparable to that for pure urania and zirconia in the same condition. Considering the behaviour of the stoichiometric oxides in argon atmosphere, such a maximum melting is certainly unexpected, even though also the solidus in argon shows a slight increment at 0.5 mol fraction of zirconia. A possible explanation of the high melting point for the sample with 0.5 mol fraction of zirconia can be the presence of more than one liquid phase or a liquid phase and an unmelted solid. The presence of different phases would be confirmed by the XRD analysis result on the starting materials, which displayed cubic and tetragonal phases corresponding to the structure of respectively urania and zirconia for the sample containing less than 0.8 mol fraction of zirconia.

On the other hand, XRD analysis also showed that in many cases the solid material, obtained by fast quenching from the liquid,

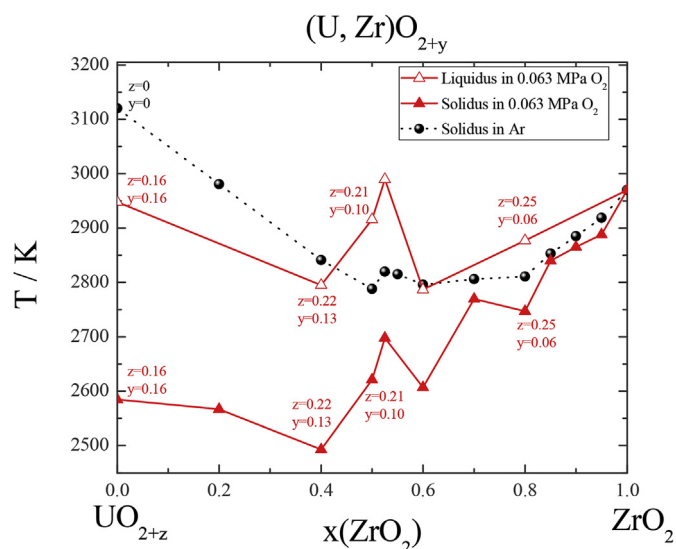


Fig. 7. The  $\text{UO}_{2+z}\text{-ZrO}_2$  phase diagram between 2500 and 3200 K. The approximate liquidus point of the composition  $\text{UO}_{2.16}$  is reported from the calculated U–O phase diagram of Guéneau et al. [27].  $z$  and  $y$  values are obtained from the current XANES analysis on samples laser melted in pressurised air.

**Table 4**

Oxygen potential dependence on the uranium dioxide hyperstoichiometry,  $z$ , at the solidification temperatures observed in this work, according to Lindemer and Besmann's model [28]. Ideal solution contribution and the energetic stabilisation effect of zirconia on the oxygen potential of the mixture are also reported for each composition in this table. The oxygen potential values are typically affected by a  $\pm 10000$  J mol<sup>-1</sup> uncertainty. They should therefore be considered as best estimates.

	$z$	T (K)	Oxygen potential (J mol <sup>-1</sup> )	Total ZrO <sub>2</sub> stabilisation effect (J mol <sup>-1</sup> )	Ideal solution effect (J mol <sup>-1</sup> )	Pure ZrO <sub>2</sub> stabilisation effect (J mol <sup>-1</sup> )
UO <sub>2.16</sub>	0.16	2585	-14692	0	0	0
U <sub>0.6</sub> Zr <sub>0.4</sub> O <sub>2.13</sub>	0.22	2493	24642	-34219	-14117	-20102
U <sub>0.5</sub> Zr <sub>0.5</sub> O <sub>2.10</sub>	0.21	2621	31944	-42012	-15104	-26908
U <sub>0.2</sub> Zr <sub>0.8</sub> O <sub>2.06</sub>	0.25	2747	96644	-107196	-11428	-95768

contained various phases. Mixtures of quenched tetragonal crystallites were observed in Zr-rich compositions melted under argon, whereas melting under air mostly led to quenched cubic phases except for the highly Zr-rich composition which were mainly tetragonal. Only in these compositions most abundant in Zr, traces of a monoclinic phase were also recorded. Despite the co-existence of these phases in the quenched material, it is worth mentioning that solid-solid phase changes, such as the cubic-tetragonal and tetragonal-monoclinic transitions, were not directly observed in the current thermograms, certainly due to the large cooling rates (often exceeding 10<sup>5</sup> K/s) produced in the laser-heating experiments. The present XRD results can nonetheless be useful in the analysis of corium formation. For example, observing that samples with  $x(\text{ZrO}_2) \leq 0.8$  contained at least two phases having widely different zirconia contents, it seems quite probable that the LOCA melted core could also solidify into two phases with widely different uranium content.

In summary, liquefaction temperatures well below the assessed UO<sub>2.00</sub> melting point (3130 K  $\pm$  20 K) [24–27] can be expected for the fuel-cladding assembly in oxidising conditions. In particular, this is true for the compositions between U<sub>0.6</sub>Zr<sub>0.4</sub>O<sub>2+y</sub> and U<sub>0.4</sub>Zr<sub>0.6</sub>O<sub>2+y</sub>, which have been identified as most representative of the real corium formed in a LOCA accident, for example, by the VERCORS [29] and PHEBUS FP [30] tests. For example, U<sub>0.6</sub>Zr<sub>0.4</sub>O<sub>2.13</sub> was observed here to solidify only at 2493 K (Table 1).

The VERCORS and PHEBUS FP tests [15] [29] [30], were performed in the previous decade on UO<sub>2</sub>-ZrO<sub>2</sub> mixtures on a scale closer to that of a real LOCA accident in a Nuclear Power Plant. The composition of the quenched melts was then locally mapped by Electron Micro-Probe Analysis (EMPA), providing semi-quantitative data for the U/Zr and the oxygen-to-metal ratios. These test evidenced themselves by liquefaction (or collapse) of the LWR nuclear fuel rod under oxidising conditions at relatively low temperatures, i.e. 200–300 K below the eutectic temperature of the UO<sub>2</sub>-ZrO<sub>2</sub> phase diagram, and at O/M ratios sometimes much larger than 2.00. Thus the composition mentioned above [U<sub>0.6</sub>Zr<sub>0.4</sub>O<sub>2.14</sub>] compares quite closely in terms of U/Zr ratio with a composition of the corium pool from the degraded FPT2 Phebus bundle: [(U,Pu,Th)<sub>0.56</sub>Zr<sub>0.42</sub>(-Fe,Cr,Mo)<sub>0.02</sub>]O<sub>2.22</sub> [30]. In FPT2 the O/M ratio of the corium pool was quite high. For the FPT1 bundle a similar U/Zr ratio was observed in the overall corium pool [U<sub>0.52</sub>Zr<sub>0.44</sub>(Fe,Cr)<sub>0.04</sub>O<sub>2+y</sub>] but the hyperstoichiometry of  $y$  was slight ( $<0.01$ ) [31]. Further analyses found higher stoichiometry locally but a near-stoichiometry value more often. It would seem to vary with the corium's position in the degraded fuel bundle and obviously to the exact atmospheric conditions that position had been exposed to during the test. Nevertheless it is clear that oxidising conditions in the PHEBUS tests can lower the melting point of U-containing corium and enhance the degradation processes. VERCORS tests at CEA concentrated more on the fission product release in various atmospheres and in their publications [32–34] concluded that oxidising conditions often resulted in a far higher release of volatile fission products, especially those such as Sb, or Ru and Mo that have

volatile oxide forms; U was also found to have higher releases. This indicates that the oxidation processes of corium are not just limited to the UO<sub>2</sub> fuel but also include certain key fission products.

In comparison, the present investigation, although performed on a much smaller scale, also provides quantitative (XANES) oxygen-to-metal data on melted and quenched samples with a pre-defined U/Zr ratio. The current results constitute therefore sound experimental data in the ternary U-Zr-O vs. T phase diagram. Incidentally, their qualitative agreement with the results of the PHEBUS FP corium pool composition is acceptable, despite the essential differences already highlighted between the present approach and those large-scale tests. It can be noticed, however, that the solidus temperatures measured for the three uranium-rich oxidised compositions (U<sub>0.5</sub>Zr<sub>0.5</sub>O<sub>2.10</sub>, U<sub>0.6</sub>Zr<sub>0.4</sub>O<sub>2.13</sub>, U<sub>0.8</sub>Zr<sub>0.2</sub>O<sub>2+y</sub>) and pure UO<sub>2.16</sub> are rather similar within the uncertainty bands reported in Table 1 and in Fig. 6. Therefore, a eutectic surface is likely to exist in this compositional range of the ternary U-Zr-O phase diagram. Also this result is qualitatively compatible with the CALPHAD optimisation published by Chevalier et al. [14] by Barrachin et al. [15] and, more recently, by Quaini [16]. In comparing the current results with Barrachin's phase boundary optimisation, one should also take into account the fact that CALPHAD phase boundaries were calculated for an equilibrium system at atmospheric pressure, whereas experimental data were measured in this work under a slightly over-pressurised buffer gas (0.3 MPa). Although small, phase boundary variations induced by this pressure difference might be relevant. In conclusion, it is soundly confirmed that an even relatively small change of the oxygen-to-metal ratio can have considerable consequences on the liquefaction temperatures in typical mixed uranium-zirconium oxides that are produced in a NPP core meltdown accident.

## 5. Conclusions

The application of a quasi-containerless laser heating method together with an improved material preparation via a sol-gel method has yielded new results on the melting transition in the U-Zr-O system in the vicinity of the pseudo-binary UO<sub>2</sub>-ZrO<sub>2</sub> system.

Results suggest that a minimum melting point exists in the pseudo-binary UO<sub>2</sub>-ZrO<sub>2</sub> plane, at a composition near U<sub>0.4</sub>Zr<sub>0.6</sub>O<sub>2</sub> at a temperature close to 2800 K under inert conditions.

New experimental data on the melting transition in strongly oxidising conditions are presented, that are useful in simulating an accident environment where the hyperstoichiometric fuel interacts with oxidised Zircaloy (i.e., mostly ZrO<sub>2</sub>) and may melt several hundreds of degrees K below the melting point of the same material in an inert or reducing atmosphere.

XANES analysis was very useful for the determination of the oxidation state of uranium and the total oxygen-to metal ratio in the hyper-stoichiometric compositions formed after laser heating under oxidising conditions. A molar oxygen-to-metal ratio (O/M) up to 2.16 was reached in pure UO<sub>2</sub> laser melted in air, in fair

agreement with oxygen potential calculations based on the Lindemer and Besmann's earlier equilibrium thermodynamic modeling. This agreement shows that the O/U ratio at the solidification point was reasonably preserved during quenching to ambient temperature, at least within the resolution limits of the current material characterisation techniques. This observation, extended to mixed hyperstoichiometric urania-stoichiometric zirconia compositions, shows that increasing the zirconia content has the effect of stabilising increasingly higher O/U values at an oxygen potential much lower than the one expected for the same O/U ratios in pure urania. Thus the hyperstoichiometry can be effectively attributed just to the urania content of the composition (i.e. it can be considered as  $\text{UO}_{2+y}\text{ZrO}_2$ ).

Among other compositions, the liquefaction/solidification behaviour of an  $\text{U}_{0.6}\text{Zr}_{0.4}\text{O}_{2.13}$  sample was studied as a representative example of a typical oxidised corium composition. This latter sample was observed to solidify at a temperature as low as 2493 K. It was thus confirmed that a relatively small change of the stoichiometry can result in considerable drop of the liquidus and solidus temperatures.

Together with the material characterisation performed before and after melting by SEM and XRD, the current XAS analysis permitted the identification and understanding of the phase separation processes in relation with the phase diagram.

Moreover, the present XRD results can be useful in the analysis of corium formation. For example, observing that samples with  $x(\text{ZrO}_2) \leq 0.8$  always contain at least two phases having widely different zirconia contents, one may suppose that a melted core produced in a LOCA could also solidify into two phases with widely different urania content.

The current results are thus important for the comprehension of the nuclear fuel behaviour in case of an accident during which the material interaction temperatures are rapidly and substantially exceeded.

## Acknowledgements

S.M. acknowledges the EURATOM FP7 project GENTLE (contract number 323304) for supporting her stay at JRC Karlsruhe. The X-ray absorption experiments were carried out under the TALISMAN collaborative project (Grant Agreement Number 323300) under the JRP no. TALI-C04-05. The authors are thankful to the beamline scientists for their help during the XANES experiment.

E.K. acknowledges the Mobility and Training Programme for Young Researchers of the European Commission.

The Authors are indebted to D. Bouexière and P. Raison (JRC Karlsruhe) for the XRD measurements, to W. Heinz and M. Sheindlin (JRC) for their early and fundamental contribution to the development of the current experimental technique, and to R. Konings and J. Somers (JRC) for the useful scientific discussions.

## References

- [1] D. Jacquemain, Nuclear power reactor core melt accidents, State Knowl. EDP Sci. IRSN (2015). ISBN: 978-2-7598-1835-8.
- [2] P. Hofman, D. Kerwin-Peck,  $\text{UO}_2/\text{Zircaloy-4}$  chemical interactions from 1000 to 1700°C under isothermal and transient temperature conditions, J. Nucl. Mater. 124 (1984) 80–105. [http://dx.doi.org/10.1016/0022-3115\(84\)90013-8](http://dx.doi.org/10.1016/0022-3115(84)90013-8).
- [3] P.E. Evans, The system  $\text{UO}_2\text{--ZrO}_2$ , J. Am. Ceram. Soc. 43 (1960) 443–446. <http://dx.doi.org/10.1111/j.1151-2916.1960.tb13695.x>.
- [4] W.A. Lambertson, M.H. Mueller, Uranium oxide phase equilibrium systems: III,  $\text{UO}_2\text{--ZrO}_2$ , J. Am. Ceram. Soc. 36 (1953) 365–368. <http://dx.doi.org/10.1111/j.1151-2916.1953.tb12819.x>.
- [5] G.M. Wolton, Solid-phase transitions in the  $\text{UO}_2\text{--ZrO}_2$  system, J. Am. Chem. Soc. 80 (1958) 4772–4775. <http://dx.doi.org/10.1021/ja01551a005> [18].
- [6] A. Skokan, High temperature phase relations in the U–Zr–O system, Karlsruhe, in: Proc. 5th international meeting on thermonuclear reactor safety, September 1984, pp. 9–13.
- [7] P. Piluso, G. Trillon, C. Journeau, The  $\text{UO}_2\text{--ZrO}_2$  system at high temperature (T > 2000 K): importance of the meta-stable phases under severe accident conditions, J. Nucl. Mater. 344 (2005) 259–264. <http://dx.doi.org/10.1016/j.jnucmat.2005.04.052>.
- [8] E.C. Subbarao, Zirconia. An overview, in: A.H. Heuer, L.W. Hobbs (Eds.), Advances in Ceramics: Science and Technology of Zirconia 003, American Ceramic Society, Columbus, Ohio, 1981, pp. 1–24.
- [9] G. Teufer, The crystal structure of tetragonal  $\text{ZrO}_2$ , Acta Cryst. 15 (1962) 1187. <https://doi.org/10.1107/S0365110X62003114>.
- [10] R.N. Patil, E.C. Subbarao, Monoclinic-tetragonal phase transition in zirconia: pre-transformation and coexistence, Acta Cryst. A26 (1970) 535–542. <http://dx.doi.org/10.1107/S0567739470001389>.
- [11] P.E. Quintard, P. Barberis, A.P. Mirgorodsky, T. Merle-Mejean, Comparative lattice-dynamical study of the raman spectra of monoclinic and tetragonal phases of zirconia and hafnia, J. Am. Ceram. Soc. 85 (2002) 1745–1749. <http://dx.doi.org/10.1111/j.1151-2916.2002.tb00346.x>.
- [12] D. Manara, M. Sheindlin, W. Heinz, C. Ronchi, New techniques for high-temperature melting measurements in volatile refractory materials via laser surface heating, J. Sci. Instrum. 79 (2008) 113901–113908. <http://dx.doi.org/10.1063/1.3005994>.
- [13] L.G. Wisnyi, S.W. Pijanowski, Knolls Atomic Power Laboratory (USA) Report, KAPL, 1957, p. 1702.
- [14] P.-Y. Chevalier, E. Fischer, B. Cheynet, Progress in the thermodynamic modelling of the O–U–Zr ternary system, CALPHAD 28 (2004) 15–40. <http://dx.doi.org/10.1016/j.calphad.2004.03.005>.
- [15] M. Barrachin, P.Y. Chevalier, B. Cheynet, E. Fischer, New modelling of the U–O–Zr phase diagram in the hyper-stoichiometric region and consequences for the fuel rod liquefaction in oxidising conditions, J. Nucl. Mater. 375 (2008) 397–409. <http://dx.doi.org/10.1016/j.jnucmat.2008.02.003>.
- [16] A. Quaini, Étude thermodynamique du corium en cuve - Application à l'interaction corium/béton, Ph. D. Thesis presented at the University of Grenoble-Alpes, 2016.
- [17] F. De Bruycker, K. Boboridis, R.J.M. Konings, M. Rini, R. Eloiirdi, C. Guéneau, N. Dupin, D. Manara, On the melting behaviour of uranium/plutonium mixed dioxides with high-Pu content: a laser heating study, J. Nucl. Mater. 419 (2011) 186–193. <http://dx.doi.org/10.1016/j.jnucmat.2011.08.028>.
- [18] D. Manara, R. Böhrer, L. Capriotti, A. Quaini, Z. Bao, K. Boboridis, L. Luzzi, A. Janssen, P. Pöml, R. Eloiirdi, R.J.M. Konings, On the melting behaviour of calcium monoxide under different atmospheres: a laser heating study, J. Eur. Ceram. Soc. 34 (2014) 1623–1636. <http://dx.doi.org/10.1016/j.jeurceramsoc.2013.12.018>.
- [20] S.M. Avdoshenko, A. Strachan, High-temperature emissivity of silica, zirconia and samaria from ab initio simulations: role of defects and disorder, Model. Simul. Mater. Sci. Eng. 22 (2014) 075004–075010. <https://doi.org/10.1088/0965-0393/22/7/075004>.
- [21] V. Petříček, M. Dušek, L. Palatinus, Crystallographic computing system JANA2006: general features, Z. fur Kristallogr. 229 (2014) 345–352.
- [22] B. Ravel, M. Newville, ATHENA, ARTEMIS, HEPHAESTUS: data analysis for X-ray absorption spectroscopy using IFEFFIT, J. Synchrotron Radiat. 12 (2005) 537–541. <http://dx.doi.org/10.1107/S0909049505012719>.
- [23] M.J. Welland, W.T. Thompson, B.J. Lewis, D. Manara, Computer simulation of non-congruent melting of  $\text{UO}_{2+x}$ , J. Nucl. Mater. 385 (2009) 358–363. <http://dx.doi.org/10.1016/j.jnucmat.2008.12.023>.
- [24] C. Guéneau, A. Chartier, L. Van Brutzel, Thermodynamic and Thermophysical properties of the actinide oxides, in reference module in materials science and materials engineering, Compr. Nucl. Mater. 2 (2012) 21–59. <http://dx.doi.org/10.1016/B978-0-08-056033-5.00009-4>.
- [25] R.E. Latta, R.E. Fryxell, Determination of solidus-liquidus temperatures in the  $\text{UO}_{2+x}$  system ( $-0.50 < x < 0.20$ ), J. Nucl. Mater. 35 (1970) 195. [http://dx.doi.org/10.1016/0022-3115\(70\)90100-5](http://dx.doi.org/10.1016/0022-3115(70)90100-5).
- [26] D. Manara, C. Ronchi, M. Sheindlin, M. Lewis, M. Brykin, Melting of stoichiometric and hyperstoichiometric uranium dioxide, J. Nucl. Mater. 342 (2005) 148–163.
- [27] C. Guéneau, N. Dupin, B. Sundman, C. Martial, J.-C. Dumas, S. Gossé, S. Chatain, F. De Bruycker, D. Manara, R.J.M. Konings, Thermodynamic modelling of advanced oxide and carbide nuclear fuels: description of the U–Pu–O–C systems, J. Nucl. Mater. 419 (2011) 145–167. <https://doi.org/10.1016/j.jnucmat.2011.07.033>.
- [28] T.B. Lindemer, T.M. Besmann, Chemical thermodynamic representation of  $\text{UO}_{2+x}$ , J. Nucl. Mater. 130 (1985) 473–488. [http://dx.doi.org/10.1016/0022-3115\(85\)90334-4](http://dx.doi.org/10.1016/0022-3115(85)90334-4).
- [29] Y. Pontillon, P.P. Malgouyres, G. Ducros, G. Nicaise, R. Dubourg, M. Kissane, M. Baichi, Lessons learnt from VERCORS tests.: study of the active role played by  $\text{UO}_2\text{--ZrO}_2\text{--FP}$  interactions on irradiated fuel collapse temperature, J. Nucl. Mater. 344 (2005) 265–273. <http://dx.doi.org/10.1016/j.jnucmat.2005.04.053>.
- [30] B. Clement, N. Hanniet-Girault, G. Repetto, D. Jacquemain, A.V. Jones, M.P. Kissane, P. von der Hardt, LWR severe accident simulation: synthesis of the results and interpretation of the first Phebus FP experiment FPT0, Nucl. Eng. Des. 225 (2003) 5–82. [http://dx.doi.org/10.1016/S0029-5493\(03\)00157-2](http://dx.doi.org/10.1016/S0029-5493(03)00157-2).
- [31] D. Bottomley, S. Schlutig, S. Brémier, M. Barrachin, A. De Bremaecker, C.T. Walker, J.-P. Glatz, D. Papaioannou, J.-L. Arnoult, D. Baudot, B. Simondi-Teisseire, R. Restani, D. Gavillet, Bundle degradation behaviour in the Phebus FP tests derived from their post irradiation examination (PIE), in: ANS 2008 ANNUAL MEETING, Embedded Topical Meeting: International Congress on

Advances in Nuclear Power Plants (ICAPP'08), June 8-12, 2008. Anaheim, California.

- [32] Paul D.W. Bottomley, Stephane Bremier, Jean-Paul Glatz, Clive T. Walker, EPMA of melted UO<sub>2</sub> fuel rods irradiated to a burn-up of 23GWd/tU, *Mikrochim. Acta* 132 (2000) 391–400, <http://dx.doi.org/10.1007/PL00021403>.
- [33] Yves Pontillon, Gérard Ducros, Behaviour of fission products under severe PWR accident conditions. The VERCORS experimental programme—Part 2: release and transport of fission gases and volatile fission products, *Nucl. Eng. Des.* 240 (2010) 1853–1866. <https://doi.org/10.1016/j.nucengdes.2009.06.024>.
- [34] Yves Pontillon, Gérard Ducros, Behaviour of fission products under severe PWR accident conditions, the VERCORS experimental programme—Part 3: release of low-volatile fission products and actinides, *Nucl. Eng. Des.* 240 (2010) 1867–1881. <https://doi.org/10.1016/j.nucengdes.2009.06.025>.

#### Further readings

- [19] D.P. DeWitt, J.C. Richmond, Thermal radiative properties of materials, in: D.P. DeWitt, G.D. Nutter (Eds.), *Theory and Practice of Radiation Thermometry*, Wiley, New York, 1988. ISBN: 978-0-471-61018-2.